Research Square

Preprints are preliminary reports that have not undergone peer review.
They should not be considered conclusive, used to inform clinical practice,
or referenced by the media as validated information.

Interfacial Structure of Silane-Modified Hollow Silica Microspheres: Alkyl-Chain-Length Effects on Char Evolution and Ablation Resistance of Ethylene–Propylene–Diene Rubber Composites

Yuyang Zhou
Yanwei Wen
Xiao Song
Quansheng Fu
Yangyang Zhang
Xin Zhao
Yajun Ding
dyj@njust.edu.cn

https://orcid.org/0000-0003-4542-861X

Research Article

Keywords: ethylene–propylene–diene rubber, hollow silica microspheres, filler–rubber interface, ablation resistance, pore structure

Posted Date: November 23rd, 2026

DOI: https://doi.org/10.21203/rs.3.rs-11670981/v1

License: This work is licensed under a Creative Commons Attribution 4.0 International License.
Read Full License

Interfacial Structure of Silane-Modified Hollow Silica Microspheres: Alkyl-Chain-Length Effects on Char Evolution and Ablation Resistance of Ethylene–Propylene–Diene Rubber Composites

Yuyang Zhou[1], Yanwei Wen[1,2], Xiao Song[1], Quansheng Fu[1], Yangyang Zhang[1], Xin Zhao[1], Yajun Ding[1]

[1] Key Laboratory for Soft Chemistry and Functional Materials of Ministry of Education, Nanjing University of Science and Technology, Nanjing 210094, China

[2] Shanghai Institute of Aerospace Chemical Application, Huzhou 313002, China

Yuyang Zhou and Yanwei Wen contributed equally to this work.

Corresponding author: Yajun Ding. Email: dyj@njust.edu.cn

Abstract

The polar surface of hollow silica microspheres (HSMs) is poorly compatible with nonpolar ethylene–propylene–diene rubber (EPDM), but its influence on residual-char evolution remains unclear. HSMs from the same batch were modified with trimethoxysilane, methyltrimethoxysilane, butyltrimethoxysilane, and octyltrimethoxysilane (OTMS) to distinguish the intrinsic protection of the hollow filler from the contribution of interfacial regulation. Interfacial measurements, molecular dynamics simulations, mechanical testing, and post-ablation characterization showed that increasing alkyl-chain length reduced surface polarity, strengthened filler–rubber association, and restricted EPDM chain mobility. These changes improved HSM dispersion and refined the pore architecture of the residual char. Compared with unmodified HSMs/EPDM, the OTMS-modified composite showed a decrease in accessible porosity from 22.9% to 17.5% and in the fraction of pore entries larger than 1000 nm from 68.2% to 39.1%, together with improved char continuity and mechanical integrity. Its mass and linear ablation rates were further reduced by 19.1% and 9.7%, respectively. These results connect pre-ablation interfacial chemistry with post-ablation pore structure and demonstrate that silane-chain-length regulation enhances the protective performance of HSM-filled EPDM composites.

Keywords: ethylene–propylene–diene rubber; hollow silica microspheres; filler–rubber interface; ablation resistance; pore structure

1. Introduction

The filler–rubber interface in particulate-reinforced elastomer composites is a critical structural parameter that governs thermal decomposition behavior and the structural evolution of the residual char. Adsorption at filler surfaces and confinement between particles alter rubber-chain mobility and the mechanical response of the interphase [1–3]. For ethylene–propylene–diene rubber (EPDM) composites filled with hollow silica microspheres (HSMs), this interface is intrinsically mismatched. The HSM surface is rich in polar Si–OH groups, whereas EPDM is weakly polar [4, 5]. Such polarity mismatch promotes filler agglomeration and weak interfacial association. The resulting heterogeneous regions develop into coarse cavities, cracks, and detachment-prone domains within the residual char upon pyrolysis. The structural quality of the post-ablation residue, including its pore architecture, continuity, and mechanical retention, therefore depends not only on the intrinsic thermal stability of the inorganic filler but also on the interfacial structure established before ablation [6, 7].

Silane modification offers a versatile route to tailor this interfacial structure and improve the compatibility between inorganic fillers and rubber matrices [8]. The chain length of the grafted alkyl groups has been shown to govern filler agglomeration, interfacial shear strength, and polymer–chain interactions under ambient conditions [9–11]. In ablation systems, silane-modified fillers have been studied mainly in silica-filled EPDM, where improved dispersion and interfacial bonding contribute to denser char layers [8]. For hollow microspheres, however, research has primarily focused on microsphere size, shell integrity, and macroscopic ablation rates [12, 13]. Whether the pre-ablation

interfacial alkyl-chain length can determine the pore architecture, continuity, and mechanical retention of the post-ablation residue remains unresolved.

In this study, HSMs from the same batch were used as a common inorganic platform, and their interfacial chemistry with EPDM was systematically tuned by varying the substituents retained at the surface. Trimethoxysilane (TMS) serves as a Si–H reference, while methyltrimethoxysilane (MTMS), butyltrimethoxysilane (BTMS), and octyltrimethoxysilane (OTMS) form an alkyl series with progressively longer methyl, butyl, and octyl groups. An unmodified-HSM control is used to distinguish the baseline protection supplied by the hollow filler from the additional contribution of surface regulation. The OTMS-modified composite exhibited simultaneous improvements in tensile strength and elongation at break, together with markedly reduced mass and linear ablation rates relative to neat EPDM. More importantly, compared with unmodified HSMs/EPDM, silane regulation decreased accessible porosity and significantly reduced the fraction of coarse pore entries, indicating a more continuous and mechanically retained residual layer. These results show that HSMs supply lightweight inorganic protection, while surface-structure regulation further determines whether this inorganic phase can be uniformly incorporated and retained within the ablation residue through more effective filler–rubber coupling. A direct connection is thus established between pre-ablation interface design and post-ablation residual-layer structure.

2. Experimental

2.1. Materials

Ethylene–propylene–diene rubber (EPDM, grade 4045; ethylene content, 47.0 wt%; ENB content, 5.0 wt%) was supplied by Jilin Petrochemical Co., Ltd. (China). Hollow silica microspheres (HSMs) were supplied by Ningbo Teli Technology Co., Ltd. (China). Trimethoxysilane (TMS), methyltrimethoxysilane (MTMS), butyltrimethoxysilane (BTMS), and octyltrimethoxysilane (OTMS) (Aladdin; purity ≥98%, GC) were purchased from Nanjing Juyou (China). Aramid fibers (AFs, PS-3), zinc oxide (ZnO), benzoxazine resin (BA, CG2400), sulfur (S), and dicumyl peroxide (DCP) were purchased from Shanghai Jinghua Chemical Reagent Co., Ltd. (China). Stearic acid (StA), anhydrous ethanol, and cyclohexane were purchased from Sinopharm Chemical Reagent Co., Ltd. (China). Tetramethylthiuram disulfide (TMTD), diiodomethane, acetone, and hydrochloric acid were purchased from Nanjing Juyou (China) and Shanghai Titan Scientific Co., Ltd. (China). Deionized water was prepared in the laboratory.

2.2. HSM surface modification

The preparation of silane-modified HSMs involved surface hydroxylation followed by silane grafting, as illustrated in Online Resource 1 (Fig. S1). Firstly, HSMs (10.0 g) were dispersed in 200 mL of 0.1 mol/L hydrochloric acid solution, ultrasonicated for 10 min, and stirred at room temperature for 2 h. After filtration and washing with deionized water until neutral, the particles were vacuum-dried at 60 °C for 12 h to obtain HSMs–OH. Then, a fixed molar amount of silane precursor (0.0147 mol per 10.0 g HSMs, corresponding to 1.80 g of TMS, 2.00 g of MTMS, 2.62 g of BTMS, or 3.45 g of OTMS) was added into 100 mL of ethanol/water mixture (90:10, v/v). The pH was adjusted to 4.5 using hydrochloric acid, followed by prehydrolysis for 30 min. Subsequently, HSMs–OH (10.0 g) was introduced and refluxed at 78 °C for 6 h after ultrasonication for 10 min. The products were collected by filtration, washed with ethanol and acetone, and vacuum-dried at 60 °C for 12 h to obtain silane-modified HSMs. TMS–HSMs, MTMS–HSMs, BTMS–HSMs, and OTMS–HSMs were prepared using the same procedure with TMS, MTMS, BTMS, and OTMS, respectively, while maintaining an identical molar amount of silane precursor.

2.3. Preparation of modified HSMs/EPDM

The silane-modified HSMs/EPDM compounds were fabricated using an LN-120 open two-roll mill (LINA Machinery Industrial Co., Ltd., China) at room temperature. The rubber formulation was as follows: EPDM, 100 phr; zinc oxide, 5 phr; stearic acid, 1 phr; silane-modified HSMs, 30 phr; dicumyl peroxide, 4.5 phr; sulfur, 1.5 phr; aramid fibers (AFs), 3 phr; tetramethylthiuram disulfide (TMTD), 1 phr; and benzoxazine resin, 15 phr. For comparison, pristine HSMs without silane modification were compounded with EPDM under identical conditions to prepare the HSMs/EPDM control. The optimum cure times (t90) of all compounds were determined by a moving-die rheometer (MDR). After mixing, the HSMs/EPDM and silane-modified HSMs/EPDM compounds were prepared by compression molding at 160 °C and 10 MPa for their respective optimum cure times (t_{90}), using an LN35T platen press (LINA Machinery Industrial Co., Ltd., China). The composites containing pristine HSMs and different silane-modified HSMs were prepared under identical conditions and denoted as HSMs/EPDM, TMS–HSMs/EPDM, MTMS–HSMs/EPDM, BTMS–HSMs/EPDM, and OTMS–HSMs/EPDM, respectively.

2.4. Characterization

Fourier-transform infrared (FTIR) measurements were conducted with a Nicolet iS50 spectrometer (Thermo Scientific). Spectra of KBr-pellet specimens were acquired between 400 and 4000 cm^{-1}. X-ray diffraction (XRD) patterns were recorded with a MiniFlex 600C diffractometer (Rigaku), while surface chemical composition was examined by X-ray photoelectron spectroscopy (XPS) using a K-Alpha instrument (Thermo Scientific).

Contact angles were determined at 20 °C with an SL200B instrument (KINO Industry Co., Ltd., China). Deionized water and diiodomethane were used as the probe liquids, with five measurements taken for each sample. The surface-energy components were calculated using the Owens–Wendt relation [14, 15]:

$$\gamma_l(1 + \cos\theta) = 2\sqrt{\gamma_s^d \gamma_l^d} + 2\sqrt{\gamma_s^p \gamma_l^p} \quad (1)$$

$$\gamma = \gamma^d + \gamma^p \quad (2)$$

Here, θ is the contact angle; γ is the total surface energy; superscripts d and p denote the dispersive and polar components, respectively; and subscripts s and l refer to the specimen and probe liquid, respectively. Surface-energy values are expressed in mJ m^{-2}.

Bound rubber refers to the rubber fraction that remains attached to the filler surface after solvent extraction and is commonly used as a measure of filler–rubber interaction strength. For bound rubber measurements, samples were enclosed in preweighed filter paper and extracted with cyclohexane at room temperature for 7 days. Fresh solvent was introduced on day 4. The extracted specimens were subsequently vacuum-dried until their mass was constant. The bound rubber content (BdR) was calculated as follows [1, 8]:

$$BdR\ (\%) = \frac{\omega_3 - \omega_2 - \omega_1 \frac{m_f}{m_f + m_r}}{\omega_1 \frac{m_r}{m_f + m_r}} \times 100 \quad (3)$$

Here, ω_1 is the initial specimen mass, ω_2 is the filter-paper mass, and ω_3 is the total mass of the filter paper and dried residue after extraction. m_f and m_r are the masses of filler and rubber, respectively, in the formulation. The initial non-rubber fraction is subtracted from the extracted residue, and the retained rubber is normalized to the initial rubber mass.

Equilibrium swelling was evaluated separately by immersing vulcanized specimens in cyclohexane at room temperature for 7 days. Surface solvent was gently removed before the swollen specimens were weighed.

Tensile measurements were conducted with a CMT-4203 universal testing machine, following ASTM D412. Dumbbell specimens were prepared with a length of 25 mm, a width of 4 mm, and a thickness of 2 mm. Tensile strength and elongation at break were obtained from five measurements and reported as averages. The same testing system was used to evaluate the compressive response of residual chars at 1 mm/min. For compression, specimens had a square cross-section measuring 5 ± 0.04 mm on each side and a height of 2 ± 0.04 mm.

Dynamic mechanical analysis (DMA) was conducted with a Q800 analyzer (TA Instruments) in tensile mode. The oscillation frequency and dynamic strain were set to 1 Hz and 0.5%, respectively.

Specimens measured 10 ± 1.0 mm in length, 4.0 ± 0.1 mm in width, and 2.0 ± 0.1 mm in thickness. Measurements covered −60 to 10 °C with a temperature ramp of 3 °C/min.

Thermogravimetric analysis (TGA) was conducted with a DTG-60 analyzer (Shimadzu) in nitrogen, from room temperature to 800 °C. A heating rate of 20 °C/min was used for the powders. The composites were analyzed at 5, 10, 20, and 40 °C/min, and the resulting data were used to calculate apparent activation energies by the Flynn–Wall–Ozawa and Kissinger methods. The Flynn–Wall–Ozawa (FWO) relation is expressed as follows [16–18]:

$$log_{10}\beta = log_{10}(\frac{AE_a}{RG(\alpha)}) - 2.315 - 0.4567\frac{E_a}{RT} \quad (4)$$

Here, β is the heating rate, A is the pre-exponential factor, E_a is the apparent activation energy, R is the gas constant, T is the absolute temperature, α is the conversion, and G(α) is the integral conversion function. At a fixed α, E_a is obtained from the slope of $\log_{10}\beta$ versus 1/T, equal to $-0.4567E_a/R$. The Kissinger relation is given by [19]:

$$ln(\frac{\beta}{T_{max}^2}) = ln(\frac{AR}{E_a}) - \frac{E_a}{RT_{max}} \quad (5)$$

Here, T_{max} is the absolute temperature at the maximum mass-loss rate in the DTG curve. E_a is obtained from the slope of $\ln(\beta/T_{max}^2)$ versus $1/T_{max}$, equal to $-E_a/R$.

Ablation measurements were conducted according to ASTM E285-80 with a ZR-323A oxyacetylene ablation apparatus. Oxygen was supplied at 1512 L/h and 0.4 MPa, and acetylene at 1116 L/h and 0.095 MPa. Specimens were cylinders measuring 30 mm in diameter and 10 mm in height. Each specimen was placed 10 mm from the nozzle and exposed to a heat flux of 4570 kW/m² for 20 s. The linear ablation rate (LAR) and mass ablation rate (MAR) were calculated from the changes in specimen thickness and mass, respectively [8]:

$$LAR = \frac{d_1 - d_2}{t} \quad (6)$$

$$MAR = \frac{m_1 - m_2}{t} \quad (7)$$

Here, d_1 and d_2 are the specimen thicknesses before and after ablation, respectively (mm); m_1 and m_2 are the specimen masses before and after ablation, respectively (g); and t is the exposure time (s). LAR and MAR are expressed in mm s^{-1} and g s^{-1}, respectively.

Scanning electron microscopy (SEM) was conducted with Sigma 360 (ZEISS) and Regulus 8100 (Hitachi) instruments operated at 20 kV. Composite specimens were fractured after cooling in liquid nitrogen, and the surfaces were gold-coated under vacuum before examination.

Raman spectra of the residual chars were recorded with a LabRAM HR Evolution spectrometer (HORIBA, Japan) using 532 nm excitation and the laser power set to 50%. The acquisition window

was 1000–2000 cm^{-1}, and the reported results represent the average of three measurements. The integrated areas of the D and G bands were used to determine A_D/A_G.

An AutoPore V 9620 mercury intrusion porosimeter (Micromeritics) was used to determine the accessible porosity and pore-entry-size distribution of the residual chars.

2.5. Molecular dynamics simulation

Molecular dynamics (MD) simulations were performed in BIOVIA Materials Studio 2023 using the COMPASS III force field to investigate the interfacial interactions between HSMs and EPDM chains. Composite models were constructed with EPDM chains of 50 repeat units (47.0 wt% ethylene, 48.0 wt% propylene, and 5.0 wt% ENB) and a hydroxylated amorphous silica surface representing the local HSM chemistry. Silane-modified models contained grafted groups with H, methyl, butyl, or octyl substituents connected through Si–O–Si linkages. After geometry optimization and five annealing cycles between 300 and 500 K, the systems were equilibrated for 1000 ps in the NVT ensemble at 300 K and then for 1000 ps in the NPT ensemble at 300 K, with a 1 fs time step, using the Andersen thermostat and Berendsen barostat. Electrostatic interactions were evaluated using the PPPM method with an accuracy of 0.0001 kcal/mol, and van der Waals interactions used atom-based summation with a 15.5 Å cutoff and a 1 Å cubic-spline width. The binding energy, free volume, and mean-square displacement of EPDM chains were calculated from the equilibrated trajectories. Detailed model construction and force-field parameters are provided in Online Resource 1.

3. Results and Discussion

3.1. Characterization of silane-modified HSMs

The FTIR spectra of pristine and silane-modified HSMs are shown in Fig. 1(a). The spectrum of pristine HSMs exhibits characteristic absorption bands at 1100 and 801 cm^{-1}, corresponding to the asymmetric and symmetric stretching vibrations of Si–O–Si, respectively. A broad band centered at 3430 cm^{-1} and a peak at 959 cm^{-1} are assigned to the stretching vibrations of O–H and surface Si–OH groups [20]. For TMS-HSMs, a new absorption band appears at 2238 cm^{-1}, corresponding to Si–H stretching vibration [21]. The spectrum of MTMS-HSMs shows a characteristic C–H stretching band at 2961 cm^{-1}. In the cases of BTMS-HSMs and OTMS-HSMs, distinct absorption bands at 2925 and 2854–2855 cm^{-1} are attributed to the asymmetric and symmetric stretching vibrations of $–CH_2–$ groups, respectively, together with deformation vibrations at 1464–1465 cm^{-1} [22]. Furthermore, OTMS-HSMs exhibits an additional band at 721 cm^{-1}, which is assigned to the rocking vibration of long-chain $–CH_2–$ groups. These characteristic absorption bands confirm the successful introduction of H-, methyl-, butyl-, and octyl-containing silane groups onto the HSMs surface.

The TG curves separate mainly above 300 °C, where decomposition of the surface groups increases the mass loss of the modified HSMs [23, 24] (Fig. 1b). At 800 °C, unmodified HSMs retain 96.9% of their initial mass, compared with 96.21%, 95.02%, 92.92%, and 90.85% for TMS-, MTMS-, BTMS-,

and OTMS-HSMs, respectively. The corresponding mass losses are 3.1%, 3.79%, 4.98%, 7.08%, and 9.15%. Within the alkylsilane series, the greater mass loss accompanies the increase in organic-chain length. XPS shows the same increase in surface carbon content (Fig. 1c). The C/Si atomic ratio rises from 0.159 for unmodified HSMs to 0.196, 0.414, 0.896, and 1.514 for TMS-, MTMS-, BTMS-, and OTMS-HSMs, respectively. TMS produces only a small change, whereas the methyl, butyl, and octyl substituents progressively enrich the surface in carbon. OTMS-HSMs have a C/Si ratio 9.52 times that of unmodified HSMs. The higher C/Si ratios reflect the carbon introduced by the surface-bound alkyl groups [25].

The surface-energy components were calculated from water and diiodomethane contact angles using the Owens–Wendt method [14, 15]. As shown in Fig. 1d, the total surface energy decreases from 41.0 mJ m^{-2} for TMS-HSMs to 33.0, 29.7, and 27.3 mJ m^{-2} for MTMS-, BTMS-, and OTMS-HSMs, approaching the EPDM value of 26.6 mJ m^{-2}. Across the same series, the polar component falls from 4.0 to 1.5, 0.7, and 0.3 mJ m^{-2}, while the dispersive component decreases from 37.0 to 31.5, 29.0, and 27.0 mJ m^{-2}. The corresponding EPDM values are 0.16 and 26.4 mJ m^{-2}. Longer alkyl groups screen the polar silica surface and present a hydrocarbon-rich outer layer, bringing both surface-energy components closer to those of EPDM [9].

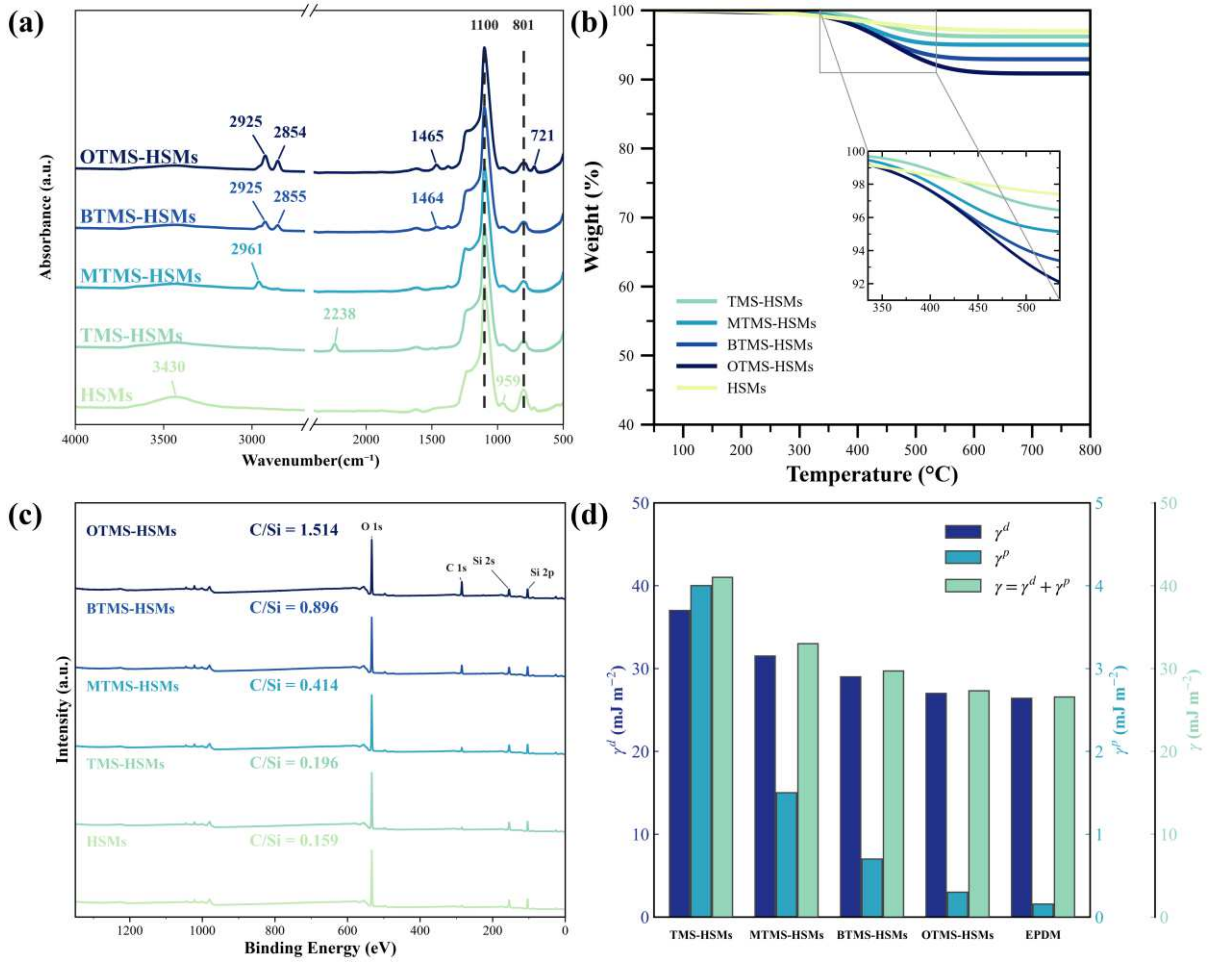


Fig. 1 FTIR spectra (a), TG curves (b), XPS (c) and surface energy (d) of silane-modified HSMs

3.2. Interfacial interaction and mechanical properties

The compatibility between HSMs and the EPDM matrix can be evaluated by the surface-energy difference parameter ΔW, calculated as follows [8, 26]:

$$\Delta W = 2(\sqrt{\gamma_f^d} - \sqrt{\gamma_r^d})^2 + 2(\sqrt{\gamma_f^p} - \sqrt{\gamma_r^p})^2 \quad (8)$$

where γ_f^d and γ_f^p represent the dispersive and polar components of HSMs, while γ_r^d and γ_r^p represent those of EPDM, respectively. When ΔW approaches zero, the filler and rubber possess more similar surface properties, which is favorable for suppressing filler aggregation [26]. As shown in Fig. 2(a), the ΔW value between unmodified HSMs and EPDM was 19.41 mJ m^{-2}, which decreased to 10.03, 6.05, 3.45, and 2.82 mJ m^{-2} for TMS-HSMs, MTMS-HSMs, BTMS-HSMs, and OTMS-HSMs, respectively. The progressive decrease in ΔW with increasing substituent-chain length indicates improved surface compatibility between HSMs and EPDM, which is attributed to the gradual shielding of the polar silanol-rich HSM surface by the organic substituents and the enhanced affinity of the longer butyl and octyl chains for the weakly polar EPDM matrix [8].

The filler–rubber interfacial interaction was further evaluated by the binding energy (E_{binding}), which was calculated by the following equation [8]:

$$E_{\text{binding}} = -E_{\text{inter}} = E_{\text{filler}} + E_{\text{matrix}} - E_{\text{total}} \quad (9)$$

where E_{total} represents the potential energy of the HSMs/EPDM composite system, while E_{filler} and E_{matrix} represent the energies of the HSMs and EPDM components, respectively. A larger positive E_{binding} value indicates stronger interfacial attraction between the filler and rubber. As shown in Fig. 2(a), the E_{binding} of HSMs/EPDM was 88.0 kcal mol^{-1}, which increased to 206, 224, 240, and 324 kcal mol^{-1} for TMS-HSMs/EPDM, MTMS-HSMs/EPDM, BTMS-HSMs/EPDM, and OTMS-HSMs/EPDM, respectively. The progressive increase in E_{binding} with increasing substituent-chain length indicates enhanced interaction between the modified HSMs and EPDM chains. This can be attributed to the larger nonpolar contact area provided by the longer alkyl substituents, which strengthens dispersive interactions with the hydrocarbon EPDM chains. Consequently, OTMS-HSMs/EPDM exhibited the highest binding energy, 3.7 times that of unmodified HSMs/EPDM.

The BdR has been used as a measure of rubber–filler interaction, with a higher bound rubber content representing stronger interaction between the rubber and filler [1, 27]. As shown in Fig. 2(b), the BdR of EPDM was 12.04%, which increased to 15.07% after the incorporation of unmodified HSMs. After silane modification, the BdR further increased to 18.01%, 21.03%, 22.96%, and 24.96% for TMS-HSMs/EPDM, MTMS-HSMs/EPDM, BTMS-HSMs/EPDM, and OTMS-HSMs/EPDM, respectively. The progressive increase in BdR with increasing substituent-chain length indicates stronger association between the modified HSMs and the EPDM matrix. This improvement can be attributed to

the enhanced compatibility of the increasingly organophilic HSM surface with EPDM, which reduces filler aggregation and facilitates more effective adsorption and physical entanglement of rubber chains around the filler surface. The effective network density of the EPDM composites obtained from equilibrium swelling [28] is also shown in Fig. 2(b). The effective network density increased from 1.188×10^{-4} mol cm^{-3} for EPDM to 2.355×10^{-4} mol cm^{-3} for HSMs/EPDM and further to 2.487×10^{-4}, 3.120×10^{-4}, 4.027×10^{-4}, and 4.344×10^{-4} mol cm^{-3} for TMS-HSMs/EPDM, MTMS-HSMs/EPDM, BTMS-HSMs/EPDM, and OTMS-HSMs/EPDM, respectively. Compared with HSMs/EPDM, the effective network density of OTMS-HSMs/EPDM increased by 84.5%. The higher network density results from the increasingly restricted mobility and swelling of EPDM chains near the modified HSM surface, indicating that longer alkyl substituents promote a more strongly constrained filler–rubber network.

The mechanical properties of the EPDM composites are presented in Fig. 2(c). The HSMs/EPDM composite exhibits a tensile strength similar to that of pristine EPDM, with the tensile strength increasing from 3.10 to 3.21 MPa. After silane modification, the tensile strength progressively increased to 4.25, 4.93, 5.80, and 6.61 MPa for TMS-HSMs/EPDM, MTMS-HSMs/EPDM, BTMS-HSMs/EPDM, and OTMS-HSMs/EPDM, respectively. In particular, the tensile strength of OTMS-HSMs/EPDM increased by 113.2% and 105.9% compared with EPDM and HSMs/EPDM, respectively, while its elongation at break reached 924%, compared with 438% for EPDM. The improved dispersion of HSMs after silane modification promotes more uniform stress distribution. Meanwhile, the enhanced interfacial compatibility allows efficient load transfer through the filler–rubber interface without excessively restricting the bulk deformability of the EPDM chains, as reflected by the simultaneously increased tensile strength and elongation at break [27]. Fig. 2(d) and (e) depict the dynamic mechanical properties of the HSMs/EPDM composites. The storage modulus (E') describes the elastic response of the composites, while the loss factor (tanδ) represents the ratio of the loss modulus (E'') to the storage modulus:

$$\tan\delta = \frac{E''}{E'} \tag{10}$$

As shown in Fig. 2(d), compared with pristine EPDM, the incorporation of HSMs increased E' from 28 MPa to 40 MPa at 0 °C, owing to the reinforcing effect of the rigid inorganic filler. After silane modification, E' further increased to 67–81 MPa, with OTMS-HSMs/EPDM exhibiting the highest value of 81 MPa. This increase can be attributed to the progressively enhanced interaction between the modified HSMs and the rubber matrix, which constrains more EPDM chains near the filler surface and reduces their mobility [2].

tanδ is highly sensitive to structural changes in the composites, and the peak position of tanδ is commonly used to determine the glass-transition temperature (T_g) and evaluate filler–rubber interactions [29]. As illustrated in Fig. 2(e), the tanδ peak decreased from 0.73 for EPDM to 0.59 for

HSMs/EPDM and further to 0.56, 0.54, 0.52, and 0.49 for TMS-HSMs/EPDM, MTMS-HSMs/EPDM, BTMS-HSMs/EPDM, and OTMS-HSMs/EPDM, respectively. Meanwhile, the tanδ peak gradually shifted toward higher temperature after silane modification. The progressively reduced peak height and higher T_g indicate increasingly restricted segmental motion of the EPDM chains as the silane alkyl-chain length increases [2, 8].

The molecular mobility of EPDM chains was further evaluated by the mean square displacement (MSD), with a lower MSD value indicating stronger restriction of chain motion. The MSD was calculated by the following equation [8]:

$$MSD(t) = \frac{1}{N}\sum_{i=1}^{N} \langle |r_i(t + t_0) - r_i(t_0)|^2 \rangle_{t_0} \quad (11)$$

where N is the number of selected EPDM atoms, r_i represents the position of atom i, and the brackets denote averaging over different time origins t_0. The MSD is expressed in Å² as a function of time in ps. As shown in Fig. 2(f), the MSD at 1000 ps decreased from 7.6 Å² for EPDM to 6.7 Å² for HSMs/EPDM and further to 5.8, 4.7, 3.7, and 2.6 Å² for TMS-HSMs/EPDM, MTMS-HSMs/EPDM, BTMS-HSMs/EPDM, and OTMS-HSMs/EPDM, respectively. The MSD of OTMS-HSMs/EPDM decreased by 65.8% compared with EPDM. The progressive decrease in MSD with increasing substituent-chain length indicates increasingly restricted motion of the EPDM chains. This can be attributed to the enlarged nonpolar contact area provided by the longer alkyl substituents, which strengthens dispersive interactions with EPDM chains and constrains their mobility near the HSM surface.

The cryogenically fractured surfaces of the HSMs/EPDM composites are shown in Fig. 2(g–i). As highlighted by the red circles in Fig. 2(h) and (i), the agglomerates become smaller in MTMS-HSMs/EPDM, while HSMs/EPDM exhibits obvious particle-rich agglomerates with a fractured hollow microsphere (Fig. 2(i)). In contrast, the aggregates become smaller in MTMS-HSMs/EPDM (Fig. 2(h)), while OTMS-HSMs/EPDM exhibits a more uniform distribution of HSMs with substantially reduced aggregation (Fig. 2(g)). TMS-HSMs/EPDM still contains several compact particle aggregates (Fig. S8(a)), whereas BTMS-HSMs/EPDM exhibits predominantly isolated or loosely associated microspheres with substantially fewer dense clusters (Fig. S8(b)). With increasing substituent-chain length, the improved compatibility between the HSM surface and EPDM suppresses filler reagglomeration and promotes a more homogeneous dispersion [30]. Furthermore, a fractured hollow microsphere can be observed within the agglomerated region of HSMs/EPDM (Fig. 2(i)). The concentrated particle–particle contacts within the agglomerate generate localized stress on the thin silica shells, increasing their susceptibility to fracture during processing and cryogenic fracture. The reduction of such particle-rich regions after silane modification therefore decreases local structural defects and facilitates more uniform stress transfer through the EPDM matrix.

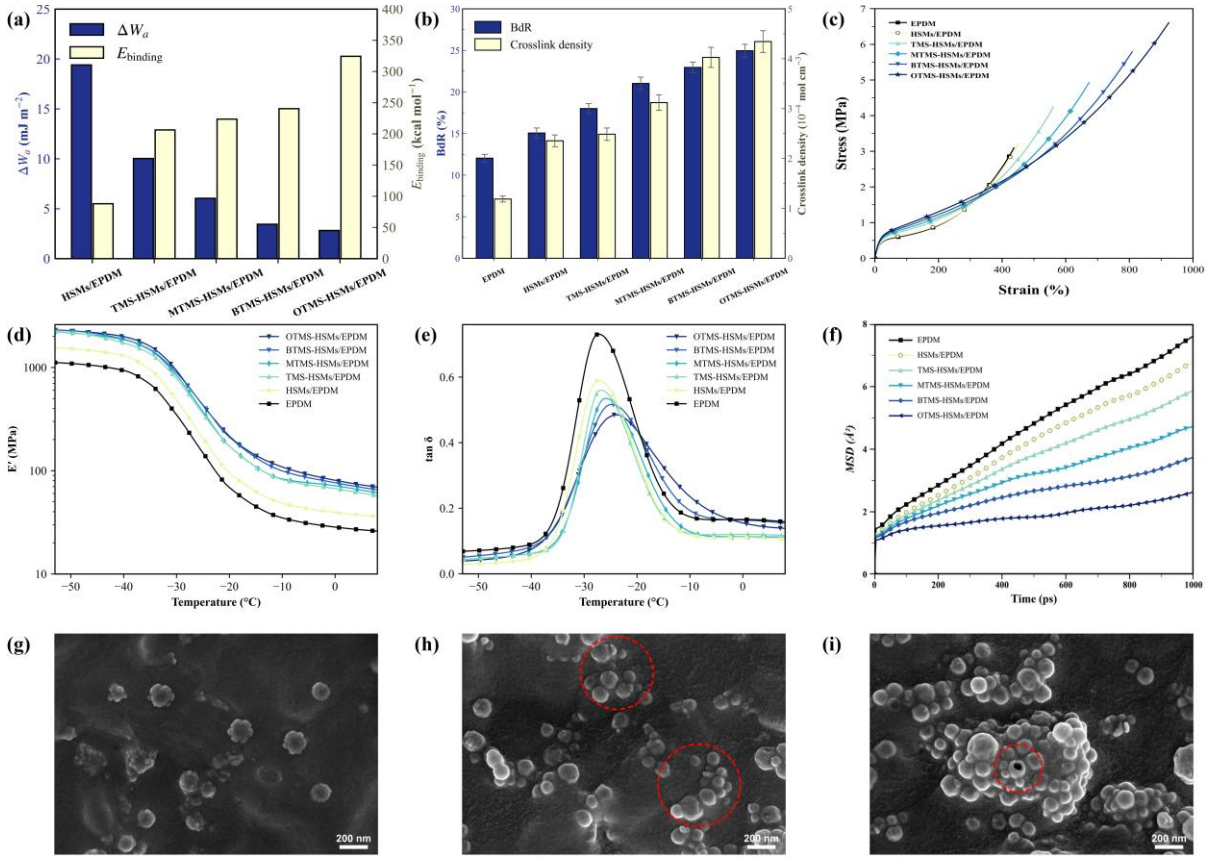


Fig. 2 ΔW and $E_{binding}$ between HSMs and EPDM (a), BdR and effective network density (b), tensile stress–strain curves (c), E′ versus temperature curves (d), tanδ versus temperature curves (e), MSD of EPDM chains (f), and SEM images of the cryogenically fractured surfaces of OTMS-HSMs/EPDM (g), MTMS-HSMs/EPDM (h), and HSMs/EPDM (i)

3.3. Thermal decomposition behavior and apparent activation energy

The composites decompose mainly between 420 and 480 °C, following a small initial mass loss (Fig. 3a,b). Adding HSMs shifts the main decomposition region slightly toward higher temperature, and silane modification extends this shift. The modified composites also leave similar residue yields, suggesting that the amount of grafted silane is relatively low compared to the bulk HSM content, and the primary decomposition pathway of the EPDM matrix remains largely unchanged. The principal change is therefore a delay in the main mass-loss process, rather than any appreciable change in residue yield.

The apparent activation energy was calculated using the Flynn–Wall–Ozawa (FWO) method [16–18] over a conversion range of α = 0.20–0.60 (Fig. 3c). EPDM and HSMs/EPDM give values of 254.1–256.7 kJ mol^{-1}. Modification with TMS and MTMS increases these values, while BTMS-HSMs/EPDM and OTMS-HSMs/EPDM exhibit even higher values of 265.0–266.0 and 267.0–267.9 kJ mol^{-1}, respectively. This ordering is maintained across the conversion range, indicating that the effect of surface treatment extends throughout the main decomposition stage. Kissinger analysis [19] gives the same ordering (Fig. 3d). The values for BTMS-HSMs/EPDM and OTMS-HSMs/EPDM are 265.4 and 267.3 kJ mol^{-1}, compared with the corresponding FWO values of 266.2 and 268.1 kJ mol^{-1}.

For OTMS-HSMs/EPDM, the increase relative to EPDM is 12.1 kJ mol^{-1}, or 4.7%. Both FWO and Kissinger analyses show a gradual increase in the apparent activation energy as the filler–rubber interaction strengthens.

The higher apparent activation energies are consistent with the restriction of chain motion observed in Section 3.2. The alkyl-modified surfaces associate more strongly with EPDM, reducing segmental mobility near the microspheres [3]. This interfacial constraint provides a physical basis for both the shift of the main decomposition peak to higher temperatures and the higher apparent decomposition barrier.

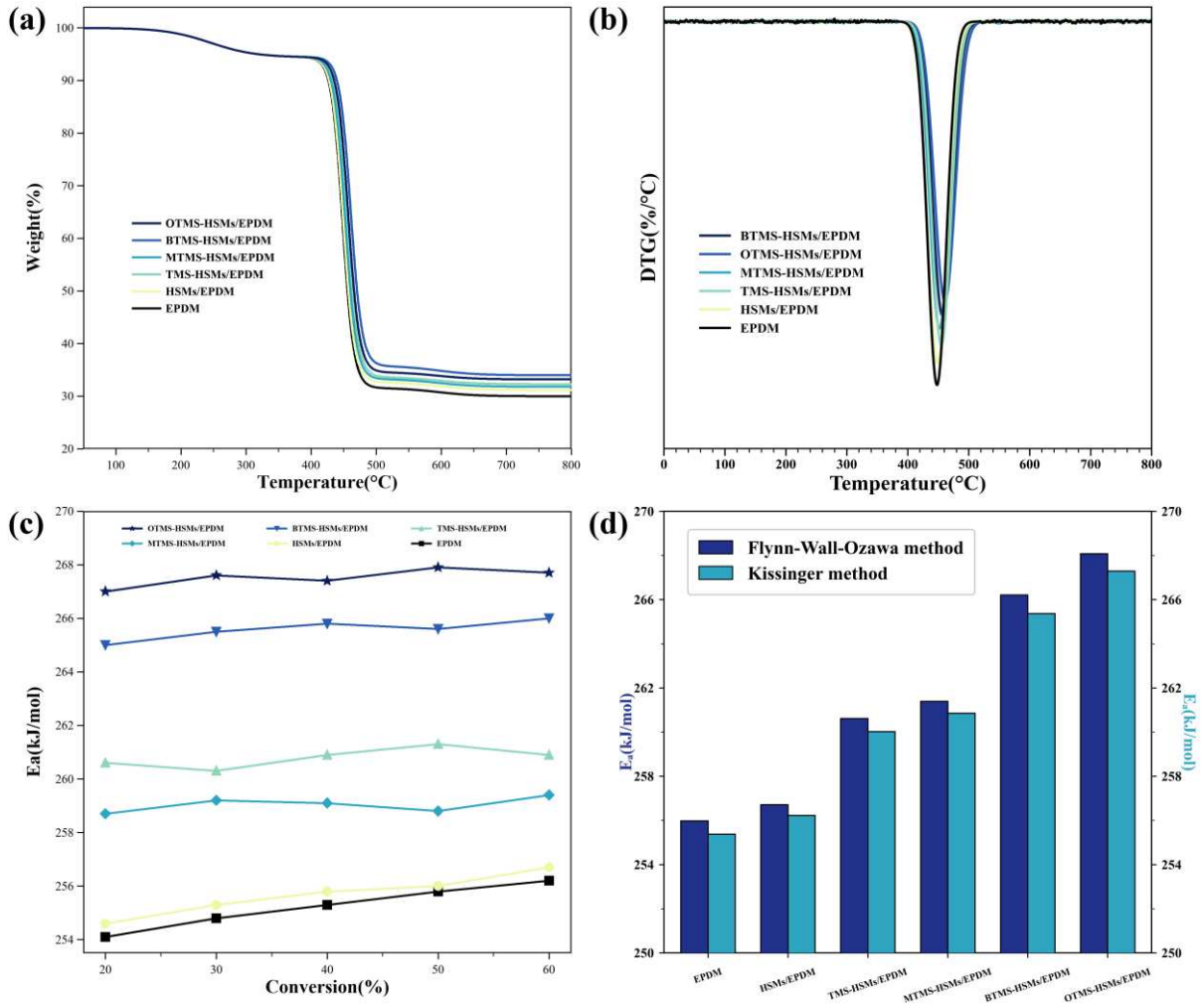


Fig. 3 TGA (a) and DTG (b) curves, conversion-dependent apparent activation energies obtained by Flynn–Wall–Ozawa method (c), and apparent activation energies of HSMs/EPDM composites calculated by Flynn–Wall–Ozawa and Kissinger methods (d)

3.4. Ablation resistance properties

The mass ablation rates (MAR) and linear ablation rates (LAR) of EPDM composites are shown in Fig. 4(a) and (b). The MAR and LAR of HSMs/EPDM composites decreased significantly compared to EPDM, from 0.159 to 0.0745 g s^{-1} and from 0.349 to 0.144 mm s^{-1}, respectively. This improvement results from the high thermal stability of HSMs, which remain in the residue and provide inorganic

support for the char layer, thereby enhancing residue retention during ablation [12, 13]. Moreover, the MAR and LAR of silane-modified HSMs/EPDM composites further decreased with increasing substituent-chain length. The MAR values of TMS-HSMs/EPDM, MTMS-HSMs/EPDM, BTMS-HSMs/EPDM, and OTMS-HSMs/EPDM decreased to 0.0717, 0.0689, 0.0632, and 0.0603 g s^{-1}, respectively, with corresponding LAR values of 0.141, 0.138, 0.132, and 0.130 mm s^{-1}. Compared with HSMs/EPDM, the MAR and LAR of OTMS-HSMs/EPDM were reduced by 19.1% and 9.7%, respectively. The progressive improvement with increasing organic-chain length is attributed to the enhanced compatibility between the modified HSM surface and the EPDM matrix, which promotes a more uniform distribution of the inorganic phase and consequently improves the stability of the residual layer.

To further evaluate the ablation resistance of the composites, the char layers were examined using SEM after ablation. As shown in Fig. 4(c1–c2), HSMs/EPDM formed a char layer with large cavities and an uneven morphology, together with obvious aggregation of HSMs in localized regions (highlighted by red circles). By comparison, MTMS-HSMs/EPDM exhibited a denser char layer with fewer large cavities and smaller HSM aggregates (Fig. 4(d1–d2)). OTMS-HSMs/EPDM demonstrated further enhancement, featuring a more continuous char layer with substantially reduced coarse defects (Fig. 4(e1)), while high-magnification SEM (Fig. 4(e2)) revealed that the microspheres were more uniformly embedded in the surrounding carbonaceous residue with minimal aggregation (highlighted by red circles). The intermediate TMS- and BTMS-modified composites show the same progressive evolution in Fig. S7: TMS-HSMs/EPDM still contains evident coarse cavities and clustered microspheres, whereas BTMS-HSMs/EPDM exhibits fewer large defects and a more dispersed distribution of HSMs. With increasing silane-chain length, the increasingly organophilic HSM surface improves dispersion in the hydrocarbon EPDM matrix, thereby reducing particle-rich heterogeneous regions before ablation. During pyrolysis, the more uniformly distributed HSMs provide dispersed inorganic support throughout the developing char layer, suppressing the formation and coalescence of large cavities and producing a denser and more continuous residual structure. This structural evolution from unmodified HSMs to the long-chain silane-modified systems is responsible for the progressive decrease in MAR and LAR.

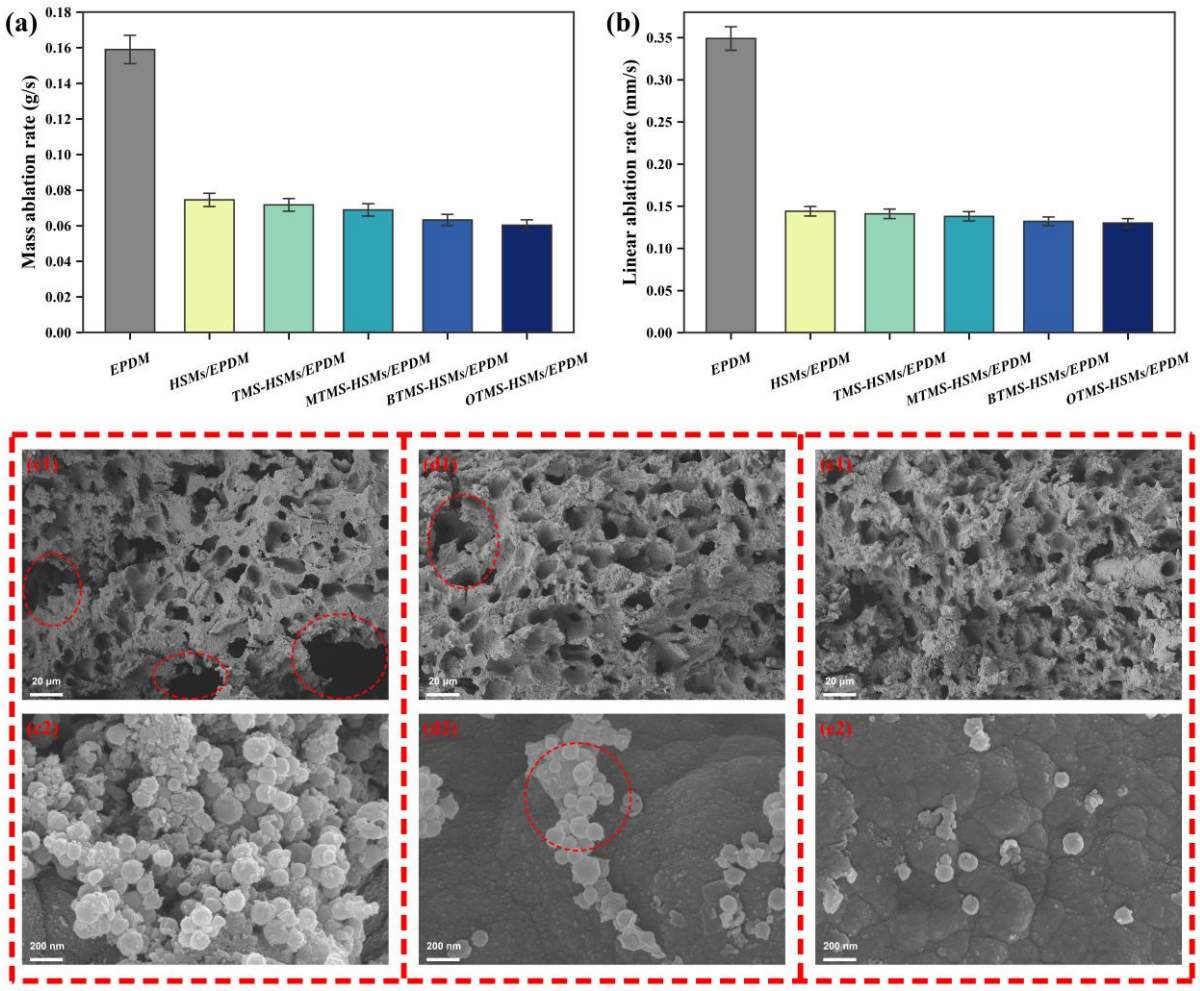


Fig. 4 MAR (a), LAR (b), and SEM images of the ablated char layers of HSMs/EPDM (c1,c2), MTMS-HSMs/EPDM (d1,d2), and OTMS-HSMs/EPDM (e1,e2) at low and high magnifications, respectively

Mercury intrusion porosimetry was employed to characterize the pore structure and porosity of the char layers [31]. As shown in Fig. 5(a), the pore-size distribution gradually shifted toward smaller sizes after silane modification. The porosity decreased from 23.8% for EPDM to 22.9% for HSMs/EPDM and further to 22.0%, 20.1%, 18.6%, and 17.5% for TMS-HSMs/EPDM, MTMS-HSMs/EPDM, BTMS-HSMs/EPDM, and OTMS-HSMs/EPDM, respectively (Fig. 5(b)). The slight decrease after adding HSMs is attributed to the thermally stable inorganic phase remaining in the residue, while the further reduction after silane modification results from the improved dispersion of HSMs in the EPDM matrix. With increasing substituent-chain length, the more uniformly distributed HSMs divide the matrix into smaller and more homogeneous pyrolysis domains, thereby restricting local gas accumulation and suppressing the growth and coalescence of cavities during decomposition. Fig. 5(c) shows the proportion of pore structures with different sizes. The fraction of large pores above 10^3 nm was 67.4% for EPDM and slightly increased to 68.2% for HSMs/EPDM, indicating that unmodified HSMs reduce the overall porosity but do not effectively suppress coarse-pore formation because of particle aggregation. After silane modification, the large-pore fraction progressively decreased to 64.3%, 50.2%, 42.4%, and 39.1%, while the fraction of pores at or below 100 nm

increased from 12.3% (HSMs/EPDM) to 32.8% (OTMS-HSMs/EPDM). With increasing substituent-chain length, improved compatibility between HSMs and EPDM suppresses particle aggregation and cavity coalescence, resulting in a finer and more compact char structure.

The stress–strain curves of the EPDM composite char layers obtained from compressive strength tests are presented in Fig. 5(d). In the initial deformation stage (strain < 40%), the curves exhibited a relatively gentle slope, which can be attributed to the compressible porous structure of the char layers. The HSMs/EPDM char layer showed a higher stress than EPDM, owing to the reinforcing effect of the rigid HSMs remaining in the char residue. After silane modification, the compressive stress progressively increased with increasing substituent-chain length, as a result of the finer pore structure and denser char layer formed by the more uniformly distributed HSMs. As the strain exceeded 40%, the stress increased rapidly, indicating progressive pore collapse and subsequent densification of the porous network [32]. At 80% strain, the compressive stresses of EPDM, HSMs/EPDM, TMS-HSMs/EPDM, MTMS-HSMs/EPDM, BTMS-HSMs/EPDM, and OTMS-HSMs/EPDM reached 13.5, 21.0, 22.1, 25.9, 31.2, and 32.3 MPa, respectively. Compared with HSMs/EPDM, the stress of OTMS-HSMs/EPDM increased by 53.8%, indicating that increasing silane-chain length progressively strengthens the load-bearing framework of the residual char.

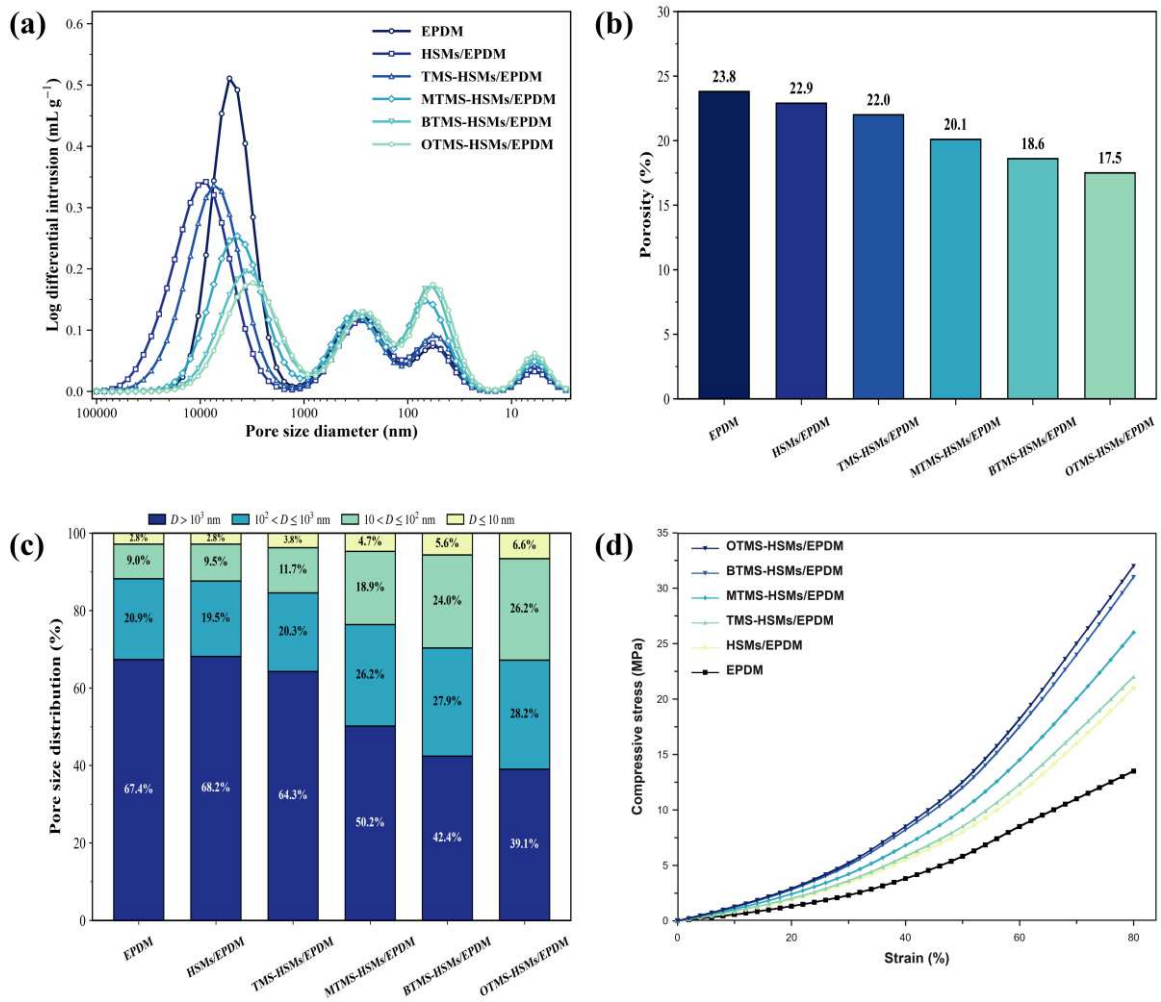


Fig. 5 Pore size distribution (a), porosity (b), proportion of pore structures with different sizes (c), and compressive stress–strain curves of the residual char layers (d)

To further investigate the carbon structure of the char layers, Raman spectra of the EPDM composites after ablation are presented in Fig. 6(a). The D band is associated with disordered and defect-containing carbon, while the G band corresponds to ordered sp^2-hybridized carbon structures [33, 34]. A lower A_D/A_G value represents a higher degree of structural ordering of the carbonaceous residue. The A_D/A_G values of EPDM and HSMs/EPDM were 1.34 and 1.31, respectively. After silane modification, the A_D/A_G values further decrease to 1.28, 1.23, 1.18, and 1.16 for TMS-HSMs/EPDM, MTMS-HSMs/EPDM, BTMS-HSMs/EPDM, and OTMS-HSMs/EPDM, respectively. The continuous decrease in A_D/A_G with increasing substituent-chain length indicates the formation of a more ordered carbon structure. This improvement can be attributed to the increasingly uniform distribution of HSMs, which reduces locally heterogeneous pyrolysis and defect-rich carbon regions and favors the development of a more continuous carbonaceous/inorganic structure.

Based on the above analyses, a possible ablation mechanism of silane-modified HSMs/EPDM composites is proposed in Fig. 6(b). When exposed to the oxyacetylene flame, the EPDM matrix undergoes rapid decomposition accompanied by the intensive release of pyrolysis gases, while the thermally stable HSMs remain in the residue and act as inorganic supporting units. For unmodified

HSMs/EPDM, the strong polarity difference between the HSM surface and EPDM causes HSM agglomeration. These particle-rich regions produce a heterogeneous pyrolysis structure, in which locally concentrated gas release promotes the growth and connection of cavities, leading to a discontinuous char layer that is readily cracked and removed under high-temperature gas erosion [35].

Silane modification alters this ablation process by regulating the initial distribution of HSMs in the matrix. With increasing substituent-chain length from TMS to OTMS, the HSM surface becomes increasingly organophilic and more compatible with the hydrocarbon EPDM matrix, resulting in progressively reduced aggregation. During ablation, the more uniformly distributed HSMs provide dispersed inorganic support throughout the developing char layer and divide the matrix into smaller and more homogeneous pyrolysis regions. This suppresses local gas accumulation and cavity coalescence, while promoting the formation of a finer, more continuous, and mechanically stable carbonaceous/inorganic framework. Therefore, increasing the silane-chain length progressively improves the integrity and structural ordering of the residual char, allowing it to more effectively resist heat penetration and erosive removal and thereby reducing both MAR and LAR [6, 7].

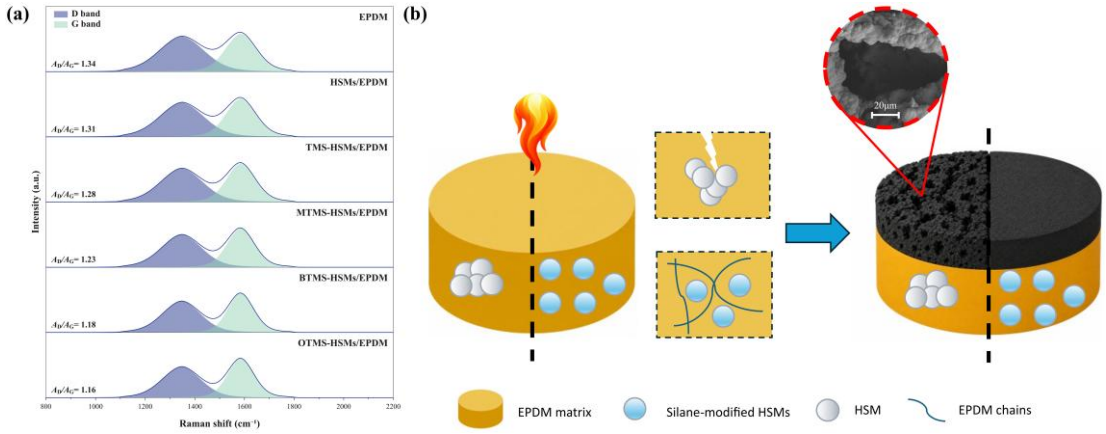


Fig. 6 Raman spectra of post-ablation char layers with fitted D- and G-band components and corresponding A_D/A_G values (a), and proposed possible ablation mechanism of silane-modified HSMs/EPDM composites (b)

4. Conclusion

Increasing the alkyl-chain length of the surface modifier improves the compatibility of HSMs with EPDM. The lower surface-energy mismatch, higher binding energy and bound rubber content, and reduced chain mobility are accompanied by better filler dispersion and enhanced mechanical performance. The OTMS-HSMs/EPDM composite reaches a tensile strength of 6.61 MPa and an elongation at break of 924%. Unmodified HSMs reduce the mass and linear ablation rates of EPDM by 53.1% and 58.7%, respectively. OTMS modification yields further reductions of 19.1% and 9.7% relative to HSMs/EPDM. It also lowers the accessible porosity from 22.9% to 17.5% and the fraction of pore entries larger than 1000 nm from 68.2% to 39.1%. The corresponding coarse-pore volume decreases by 56.2%, while the compressive stress at 80% strain rises from 21.0 to 32.3 MPa and the A_D/A_G ratio decreases from 1.31 to 1.16. These results link the interface formed before ablation to the

pore structure and mechanical stability of the residual char. HSMs supply an inorganic framework; silane modification improves its dispersion and promotes a more continuous carbonaceous/inorganic residue. Among this series, OTMS exhibits the lowest mean ablation rates, with a smaller improvement over BTMS than over the shorter-chain modifiers.

Supplementary information

Online Resource 1: Molecular dynamics simulation methods, supplementary Figs. S1–S9, and Tables S1–S2.

Declarations

Availability of data

Data will be made available on request.

Funding

No funding was received for this work.

Competing interests

The authors declare that they have no competing interests.

Authors' contributions

Yuyang Zhou: Writing – review & editing, Writing – original draft, Software, Methodology, Data curation, Conceptualization.

Yanwei Wen: Writing – review & editing, Writing – original draft, Data curation, Conceptualization.

Xiao Song: Methodology, Investigation.

Quansheng Fu: Methodology, Investigation.

Yangyang Zhang: Methodology, Data curation.

Xin Zhao: Writing – review & editing, Methodology, Investigation.

Yajun Ding: Writing – review & editing, Supervision, Resources, Project administration, Conceptualization.

All authors read and approved the final manuscript.

Acknowledgements

We acknowledge the Center of Analytical Facilities at Nanjing University of Science and Technology for providing access to characterization facilities.

References

1. Wolff S, Wang MJ, Tan EH (1993) Filler-Elastomer Interactions. Part VII. Study on Bound Rubber. Rubber Chem Technol 66:163–177. https://doi.org/10.5254/1.3538304

2. Berriot J, Montes H, Lequeux F, Long D, Sotta P (2002) Evidence for the Shift of the Glass Transition near the Particles in Silica-Filled Elastomers. Macromolecules 35:9756–9762. https://doi.org/10.1021/ma0212700

3. Starr FW, Schrøder TB, Glotzer SC (2002) Molecular Dynamics Simulation of a Polymer Melt with a Nanoscopic Particle. Macromolecules 35:4481–4492. https://doi.org/10.1021/ma010626p

4. Zhuravlev LT (2000) The surface chemistry of amorphous silica. Zhuravlev model. Colloids Surf A Physicochem Eng Asp 173:1–38. https://doi.org/10.1016/s0927-7757(00)00556-2

5. Chen G, Vahidifar A, Yu S, Mekonnen TH (2024) Sulfur Free Crosslinking of EPDM Composites via Silane Grafting and Silica Incorporation. Macromol Rapid Commun 45:2300563. https://doi.org/10.1002/marc.202300563

6. Li J, Xi K, Lv X, Li Q, Wang SX (2018) Characteristics and formation mechanism of compact/porous structures in char layers of EPDM insulation materials. Carbon 127:498–509. https://doi.org/10.1016/j.carbon.2017.10.091

7. Fu Q, Zhao X, Zhao D, Song X, Zhou Y, Zhang Y, Wang J, Jia H (2026) Designing High-Performance Ablative EPDM With a Reactive Modified Basalt Fiber Skeleton. Polym Compos 47:15622–15633. https://doi.org/10.1002/pc.71310

8. Fu Q, Zhao D, Yang Z, Song X, Zhao X, Zhang Y, Luo Y, Wang J, Jia H (2026) Bridging Scales in EPDM Composites: Experimental Validation and MD Simulation of ANFs@SiO2 Surface Modification. Polym Compos 47:5769–5780. https://doi.org/10.1002/pc.70525

9. Ji T, Ma C, Brisbin L, Mu L, Robertson CG, Dong Y, Zhu J (2017) Organosilane grafted silica: Quantitative correlation of microscopic surface characters and macroscopic surface properties. Appl Surf Sci 399:565–572. https://doi.org/10.1016/j.apsusc.2016.11.241

10. Kim KJ, White JL (2002) Silica surface modification using different aliphatic chain length silane coupling agents and their effects on silica agglomerate size and processability. Compos Interfaces 9:541–556. https://doi.org/10.1163/15685540260494119

11. Jiang ZX, Meng LH, Huang YD, Liu L, Lu C (2007) Influence of coupling agent chain lengths on interfacial performances of polyarylacetylene resin and silica glass composites. Appl Surf Sci 253:4338–4343. https://doi.org/10.1016/j.apsusc.2006.09.053

12. Rallini M, Puri I, Torre L, Natali M (2018) Thermal and ablation properties of EPDM based heat shielding materials modified with density reducer fillers. Compos Part A Appl Sci Manuf 112:71–80. https://doi.org/10.1016/j.compositesa.2018.05.031

13. Wang M, Chen X, Wang Y, Wu L, Zhou J, Liu L, Lin Z, Ren W, Liu C (2026) Study on the influence of hollow glass microspheres structure on the ablation performance of EPDM rubber. J Polym Res 33:195. https://doi.org/10.1007/s10965-026-04858-x

14. Owens DK, Wendt RC (1969) Estimation of the surface free energy of polymers. J Appl Polym Sci 13:1741–1747. https://doi.org/10.1002/app.1969.070130815

15. Fowkes FM (1964) Attractive forces at interfaces. Ind Eng Chem 56:40–52. https://doi.org/10.1021/ie50660a008

16. Flynn JH, Wall LA (1966) A quick, direct method for the determination of activation energy from thermogravimetric data. J Polym Sci B Polym Lett 4:323–328. https://doi.org/10.1002/pol.1966.110040504

17. Ozawa T (1965) A New Method of Analyzing Thermogravimetric Data. Bull Chem Soc Jpn 38:1881–1886. https://doi.org/10.1246/bcsj.38.1881

18. Vyazovkin S, Burnham AK, Criado JM, Pérez-Maqueda LA, Popescu C, Sbirrazzuoli N (2011) ICTAC Kinetics Committee recommendations for performing kinetic computations on thermal analysis data. Thermochim Acta 520:1–19. https://doi.org/10.1016/j.tca.2011.03.034

19. Kissinger HE (1957) Reaction Kinetics in Differential Thermal Analysis. Anal Chem 29:1702–1706. https://doi.org/10.1021/ac60131a045

20. Innocenzi P (2003) Infrared spectroscopy of sol–gel derived silica-based films: a spectra-microstructure overview. J Non-Cryst Solids 316:309–319. https://doi.org/10.1016/s0022-3093(02)01637-x

21. Somodi F, Kong CS, Santos JC, Morse DE (2015) Vesicular hydrogen silsesquioxane-mediated synthesis of nanocrystalline silicon dispersed in a mesoporous silica/suboxide matrix, with potential for electrochemical applications. New J Chem 39:621–630. https://doi.org/10.1039/c4nj01762e

22. Lagutchev AS, Song KJ, Huang JY, Yang PK, Chuang TJ (1998) Self-assembly of alkylsiloxane monolayers on fused silica studied by XPS and sum frequency generation spectroscopy. Chem Phys 226:337–349. https://doi.org/10.1016/s0301-0104(97)00263-2

23. Ghamarpoor R, Jamshidi M, Joshaghani M (2025) Hydrophobic silanes-modified nano-SiO_2 reinforced polyurethane nanocoatings with superior scratch resistance, gloss retention, and metal adhesion. Sci Rep 15:31555. https://doi.org/10.1038/s41598-025-16829-1

24. Moretto E, Fernandes JPC, Staropoli M, Rogé V, Steiner P, Duez B, Lenoble D, Thomann JS (2022) Dual-Silane Premodified Silica Nanoparticles—Synthesis and Interplay between Chemical, Mechanical, and Curing Properties of Silica–Rubber Nanocomposites: Application to Tire Tread Compounds. ACS Omega 7:17692–17702. https://doi.org/10.1021/acsomega.2c00665

25. Celik N, Sezen B, Sahin F, Ceylan A, Ruzi M, Onses MS (2023) Mechanochemical Coupling of Alkylsilanes to Nanoparticles for Solvent-Free and Rapid Fabrication of Superhydrophobic Materials. ACS Appl Nano Mater 6:14921–14930. https://doi.org/10.1021/acsanm.3c02489

26. Kaelble DH (1970) Dispersion-Polar Surface Tension Properties of Organic Solids. J Adhes 2:66–81. https://doi.org/10.1080/0021846708544582

27. Sun Z, Huang Q, Zhang L, Wang Y, Wu Y (2017) Tailoring silica–rubber interactions by interface modifiers with multiple functional groups. RSC Adv 7:38915–38922. https://doi.org/10.1039/C7RA07321F

28. Flory PJ, Rehner J (1943) Statistical Mechanics of Cross-Linked Polymer Networks II. Swelling. J Chem Phys 11:521–526. https://doi.org/10.1063/1.1723792

29. Basu D, Das A, Wang DY, George JJ, Stöckelhuber KW, Boldt R, Leuteritz A, Heinrich G (2016) Fire-safe and environmentally friendly nanocomposites based on layered double hydroxides and ethylene propylene diene elastomer. RSC Adv 6:26425–26436. https://doi.org/10.1039/C5RA27444C

30. Das S, Chattopadhyay S, Dhanania S, Bhowmick AK (2020) Improved dispersion and physico-mechanical properties of rubber/silica composites through new silane grafting. Polym Eng Sci 60:3115–3134. https://doi.org/10.1002/pen.25541

31. Rouquerol J, Baron G, Denoyel R, Giesche H, Groen J, Klobes P, Levitz P, Neimark AV, Rigby S, Skudas R, Sing K, Thommes M, Unger K (2012) Liquid intrusion and alternative methods for the characterization of macroporous materials (IUPAC Technical Report). Pure Appl Chem 84:107–136. https://doi.org/10.1351/PAC-REP-10-11-19

32. Pham TN, Samikannu A, Kukkola J, Rautio AR, Pitkänen O, Dombovari A, Lorite GS, Sipola T, Toth G, Mohl M, Mikkola JP, Kordas K (2014) Industrially benign super-compressible piezoresistive carbon foams with predefined wetting properties: from environmental to electrical applications. Sci Rep 4:6933. https://doi.org/10.1038/srep06933

33. Tuinstra F, Koenig JL (1970) Raman Spectrum of Graphite. J Chem Phys 53:1126–1130. https://doi.org/10.1063/1.1674108

34. Ferrari AC, Robertson J (2000) Interpretation of Raman spectra of disordered and amorphous carbon. Phys Rev B 61:14095–14107. https://doi.org/10.1103/physrevb.61.14095

35. Liu Y, Yang S, He G, Li J (2016) An overall ablation model of ethylene-propylene-diene monomer based on porous characteristics in char layer. Adv Mech Eng 8:1687814016632415. https://doi.org/10.1177/1687814016632415

Supplementary Files

This is a list of supplementary files associated with this preprint. Click to download.

- ESM1.docx